

See discussions, stats, and author profiles for this publication at: <https://www.researchgate.net/publication/256458003>

# Nanoalloying Effect in the Preferential Oxidation of CO over Ir–Pd Catalysts

ARTICLE *in* ACS CATALYSIS · AUGUST 2012

Impact Factor: 9.31 · DOI: 10.1021/cs3003325

CITATIONS

12

READS

52

4 AUTHORS, INCLUDING:



**Franck Morfin**

French National Centre for Scientific Research

87 PUBLICATIONS 908 CITATIONS

SEE PROFILE



**Jean-Luc Rousset**

Claude Bernard University Lyon 1

148 PUBLICATIONS 2,106 CITATIONS

SEE PROFILE



**Laurent Piccolo**

French National Centre for Scientific Research

67 PUBLICATIONS 1,081 CITATIONS

SEE PROFILE

# Nanoalloying Effect in the Preferential Oxidation of CO over Ir–Pd Catalysts

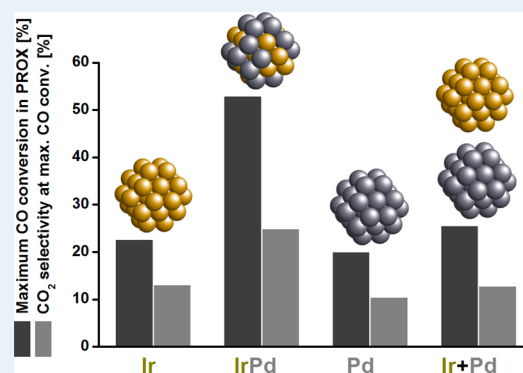
F. Morfin, S. Nassreddine, J. L. Rousset, and L. Piccolo\*

IRCELYON, Institut de recherches sur la catalyse et l'environnement de Lyon, UMR 5256 CNRS & Université Lyon 1, 2 Avenue Albert Einstein, F-69626 Villeurbanne, France

## Supporting Information

**ABSTRACT:** H<sub>2</sub>-free CO oxidation and preferential CO oxidation in the presence of H<sub>2</sub> (PROX) have been studied on Ir<sub>100-x</sub>Pd<sub>x</sub> nanoalloys ( $x = 0, 11, 45, 89$ , and 100) supported on alumina or amorphous silica–alumina. The catalysts were prepared by impregnation of acetylacetonates and characterized by transmission electron microscopy, energy-dispersive X-ray spectroscopy, and X-ray photoelectron spectroscopy. It is shown that, depending on the temperature conditions, Ir-rich catalysts undergo oxidation or reduction, leading to complex reaction kinetics upon heating or cooling. The surface acidity of the support does not significantly affect the CO oxidation performances, but decreases the CO PROX activity due to the probable promoting role of basic OH groups in this reaction. In addition, although the H<sub>2</sub>-free CO oxidation and the PROX turnover frequencies increase with the Pd content, the CO<sub>2</sub> selectivity of Ir<sub>100-x</sub>Pd<sub>x</sub> catalysts ( $x = 11$  and 45) is found superior to those of Ir catalysts, Pd catalysts, and an Ir + Pd mechanical mixture. Moreover, the selectivity of these catalysts is retained at higher temperatures and the CO conversion is higher. This synergistic alloying effect is discussed in terms of ligand effect within the hypothesized Ir@Pd core-shell structure and Ir-induced inhibition of hydride formation.

**KEYWORDS:** CO oxidation, PROX, iridium, palladium, nanoalloys, bimetallic catalysts



## 1. INTRODUCTION

The preferential oxidation of CO (PROX) is a possible way to eliminate CO impurities in hydrogen-rich streams, making it promising for on-board proton-exchange membrane fuel cell applications, which use hydrogen produced by steam reforming.<sup>1,2</sup> Since the late 1990s, the PROX reaction has been investigated on supported platinum-group metals, supported gold, and transition metal oxides such as CuO–CeO<sub>2</sub>. Among the metals, Pt (possibly promoted by Fe, Co, Ru, Sn, ...) has been a widely studied candidate because it is the fuel cell standard catalyst.<sup>1</sup> Conversely, few groups have focused on Pd-based catalysts<sup>3–11</sup> and even less on Ir-based ones,<sup>7,8,12–14</sup> despite the fact that they are both efficient metals for H<sub>2</sub>-free CO oxidation. All the comparative studies agree on the better performances of Pt<sup>4–9</sup> and Ir<sup>7,8</sup> over those of Pd in PROX.

It has been long known that metal alloying can reinforce the catalytic activity, selectivity, or stability of the parent metals.<sup>15,16</sup> However, a frequent limitation of the works dealing with bimetallic catalysts is the poor direct investigation of the nanoparticle structure, allowing one to determine if the particles are themselves bimetallic or whether monometallic particles coexist.<sup>17</sup> In a recent study<sup>18</sup> using high-resolution transmission electron microscopy (HRTEM) and single-particle energy dispersive X-ray (EDX) spectroscopy, we have shown that the Pd concentration of Ir–Pd nanoparticles supported on amorphous silica–alumina (ASA) is not constant but roughly

proportional to the particle size. This lack of homogeneity originates from standard coimpregnation–reduction method through Ostwald ripening. Moreover, it has been demonstrated how the interplay between metal particle size, composition, and catalyst acidity could affect the selectivity in tetralin hydroconversion.<sup>18</sup>

It must be noted that few catalytic studies have been devoted to the Ir–Pd system, unlike to other Pd-based combinations.<sup>19</sup> This bimetallic system has been previously examined as a catalyst of the following reactions: methane combustion,<sup>20</sup> hydrogenation of benzonitrile,<sup>21</sup> ethanol oxidation,<sup>22</sup> and tetralin hydroconversion.<sup>18,23</sup> In this paper, we report on PROX over Ir–Pd nanoalloys supported on ASA and on pure alumina. It is shown that the synergy between Ir and Pd leads to an improvement of the PROX performances.

## 2. EXPERIMENTAL SECTION

### 2.1. Catalyst Preparation and Characterization.

Amorphous silica–alumina (ASA, commercial name SICAL-40, containing 40 wt % silica) was supplied by Sasol Germany. The powder (500 m<sup>2</sup> g<sup>−1</sup>) was activated by heating at 550 °C in air for 3 h. SICAL-40 exhibits a significant Brönsted acidity.<sup>24,25</sup>

Received: May 29, 2012

Revised: August 30, 2012

Published: August 31, 2012

We extensively used this support in combination with Ir, Pd, or both in previous studies.<sup>18,25–28</sup> A standard  $\gamma$ -alumina (260 m<sup>2</sup> g<sup>−1</sup>) was used in comparison with ASA to assess the possible influence of acidity in CO oxidation. The catalysts were prepared by incipient wetness (co)impregnation of the supports with Ir acetylacetonate, Ir(acac)<sub>3</sub>; or Pd acetylacetonate, Pd(acac)<sub>2</sub>, or both. These precursors (Sigma-Aldrich, purity 97%) were dissolved in toluene using the concentration needed to obtain a metal loading of 1.0 wt %. After maturation during 2 h at room temperature, the samples were dried at 120 °C overnight and reduced in a H<sub>2</sub> flow at 350–500 °C for 6 h. More details on catalyst preparation are given in refs 18 and 26.

The catalysts were characterized by inductively coupled plasma–optical emission spectrometry (ICP–OES, Activa–Horiba Jobin Yvon), X-ray photoelectron spectroscopy (XPS, Kratos Axis Ultra DLD spectrometer, 150 W Al K $\alpha$  X-ray source at 1486.6 eV), and high-resolution transmission electron microscopy combined with energy dispersive X-ray spectroscopy. For TEM, the carbon-replicated samples were observed with Jeol 2010 (200 kV, LaB<sub>6</sub> filament, 0.19 nm resolution) and 2010F (200 kV, FEG, 0.19 nm resolution) microscopes. Size histograms were obtained from the statistical treatment of the micrographs by analyzing more than 300 particles. The metal particle size was averaged over the metal surface distribution  $n_i d_i^2$  ( $n_i$  is the number of particles in the diameter range  $d_i$ ).<sup>27</sup> The mean size  $\langle d \rangle_{\text{surf}}$  is then given by  $\sum n_i d_i^3 / \sum n_i d_i^2$ . For EDX, 10–100 nm and 2–5 nm diameter probes were used for groups of particles and individual particles, respectively. The latter allowed us to perform local composition analyses. The metal loadings (determined by ICP), mean metal compositions (ICP), and mean metal particle sizes (TEM) of the catalysts are reported in Table 1, which also contains the corresponding short names.

**Table 1. Characteristics of the Catalysts**

sample name <sup>a</sup>	Pd content/metal content (at %) <sup>b</sup>	metal weight/catalyst weight (wt %) <sup>b</sup>	particle size (nm) <sup>c</sup>
Ir/ASA	0	1.07	1.5 ± 0.3
Ir(Pd)/ASA	11	1.04	1.9 ± 0.5
IrPd/ASA	45	0.91	2.2 ± 0.8
(Ir)Pd/ASA	89	1.02	3.0 ± 0.9
Pd/ASA	100	0.89	4.5 ± 1.2
Ir/A	0	0.80	1.4 ± 0.3
IrPd/A	51	0.83	2 ± 1
Pd/A	100	0.81	3.1 ± 1.4

<sup>a</sup>ASA an A stand for amorphous silica–alumina and alumina, respectively. <sup>b</sup>Determined by ICP. <sup>c</sup>Determined by TEM.

**2.2. Catalytic Testing.** Each catalyst was evaluated in three reactions: the oxidation of CO, the selective oxidation of CO in the presence of H<sub>2</sub> (PROX), and the oxidation of H<sub>2</sub>. These tests were carried out at atmospheric pressure and variable temperature in a continuous flow fixed-bed reactor. The amounts of catalyst used corresponded to a constant total number of metal atoms (0.81  $\mu$ mol). The catalysts were diluted in Al<sub>2</sub>O<sub>3</sub> (Condea Puralox ScFa-215) to obtain a catalytic bed of 800 mg (height of 13 mm in the quartz U-shaped 10-mm-diameter tubular reactor). The reactant gases were mixed using mass-flow controllers (Brooks Instruments) and flowed through the reactor at a total rate of 50 mL min<sup>−1</sup>. All the high-purity (>99.995%) gases were purchased from Air Liquide. The gas mixture consisted of 2% CO + 2% O<sub>2</sub> + 96% He for

CO oxidation, 2% CO + 2% O<sub>2</sub> + 48% H<sub>2</sub> + 48% He for PROX, and 48% H<sub>2</sub> + 2% O<sub>2</sub> + 50% He for H<sub>2</sub> oxidation (all percentages are vol %). The outlet gases were analyzed online using a Varian Micro GC (CP2003).

The following test sequence was used for all samples: in situ reducing pretreatment, CO oxidation, PROX, and H<sub>2</sub> oxidation. The pretreatment consisted of the in situ reduction of the catalysts by heating under hydrogen flow (50 mL min<sup>−1</sup>) from room temperature (RT) to 400 °C at a rate of 3 °C min<sup>−1</sup>, followed by a 2 h plateau at 400 °C. The CO oxidation and PROX experiments consisted of two heating–cooling cycles (50–350–50 °C) at a rate of 80 °C h<sup>−1</sup>, and H<sub>2</sub> oxidation tests were performed using a single temperature ramp from RT to 120 at 80 °C h<sup>−1</sup>.

For a particular set of PROX experiments, direct reducing or oxidizing in situ pretreatment was used. The reducing treatment was the same as the above one. The oxidizing treatment consisted of 20% O<sub>2</sub> in He flow (30 mL min<sup>−1</sup>) from RT to 350 °C at a rate of 3.5 °C min<sup>−1</sup>, followed by a 2 h plateau at 350 °C.

### 3. RESULTS

**3.1. Structural Aspects.** Table 1 shows the characteristics of the eight samples, as determined from ICP and TEM. The target metal compositions (Ir/Pd = 0:100, 10:90, 50:50, 90:10, and 100:0 at %) and metal loadings (1.0 wt %) were reached within 10% and 20%, respectively. For both supports, the center and the width of the size distribution increase with the Pd content. The structural properties of the Ir–Pd/ASA series were investigated in detail in a previous paper.<sup>18</sup> From Ir/ASA to Pd/ASA, the mean particle size increases from 1.5 to 4.5 nm. In addition, as established from local EDX measurements, the Ir–Pd particles are bimetallic and exhibit a size–composition correlation. For the IrPd/ASA sample, the Pd concentration in a particle is roughly proportional to  $(d - 1)/4$ , where  $d$  is the particle diameter in nanometers.<sup>18</sup> The Ir–Pd/Al<sub>2</sub>O<sub>3</sub> series follows the same trends, and the nature of the support appears to have a moderate influence on the metal dispersion. This is not surprising because the SICAL-40 surface is alumina-rich.<sup>24</sup> Note that the structural characteristics of Ir/ASA have also been previously investigated by in situ X-ray diffraction<sup>26</sup> and X-ray photoelectron spectroscopy (XPS).<sup>27</sup>

**3.2. Catalyst Stability.** As mentioned above, two temperature cycles of CO oxidation (CO/O<sub>2</sub> = 2:2 vol % in He flow) were carried out, followed by two cycles of PROX (CO/O<sub>2</sub>/H<sub>2</sub> = 2:2:48 vol %) and one ascending-temperature run of H<sub>2</sub> oxidation (O<sub>2</sub>/H<sub>2</sub> = 2:48 vol %).

Figure 1 shows the CO oxidation and PROX results for Ir/ASA, IrPd/ASA, and Pd/ASA. Before addressing the catalytic performances, let us analyze the stability upon temperature cycling. Although the activity-vs-temperature behavior of Pd/ASA is stable (all four curves are superimposed in each graph), that of Ir/ASA changes along the cycles. For CO oxidation and PROX, looplike curves are seen during each cycle; however, the main change occurs after the first temperature rise: The CO oxidation light-off temperature somewhat increases (Figure 1a), whereas in PROX, the O<sub>2</sub> (Figure 1c) and H<sub>2</sub> (Figure 1d) conversion rates increase in such a way that the CO conversion decreases (Figure 1b). The behavior of IrPd/ASA is intermediate between those of Ir/ASA and Pd/ASA, with moderate changes in the conversions from one temperature ramp to another. Note that IrPd/ASA behaves somewhat differently from an Ir/ASA + Pd/ASA physical mixture

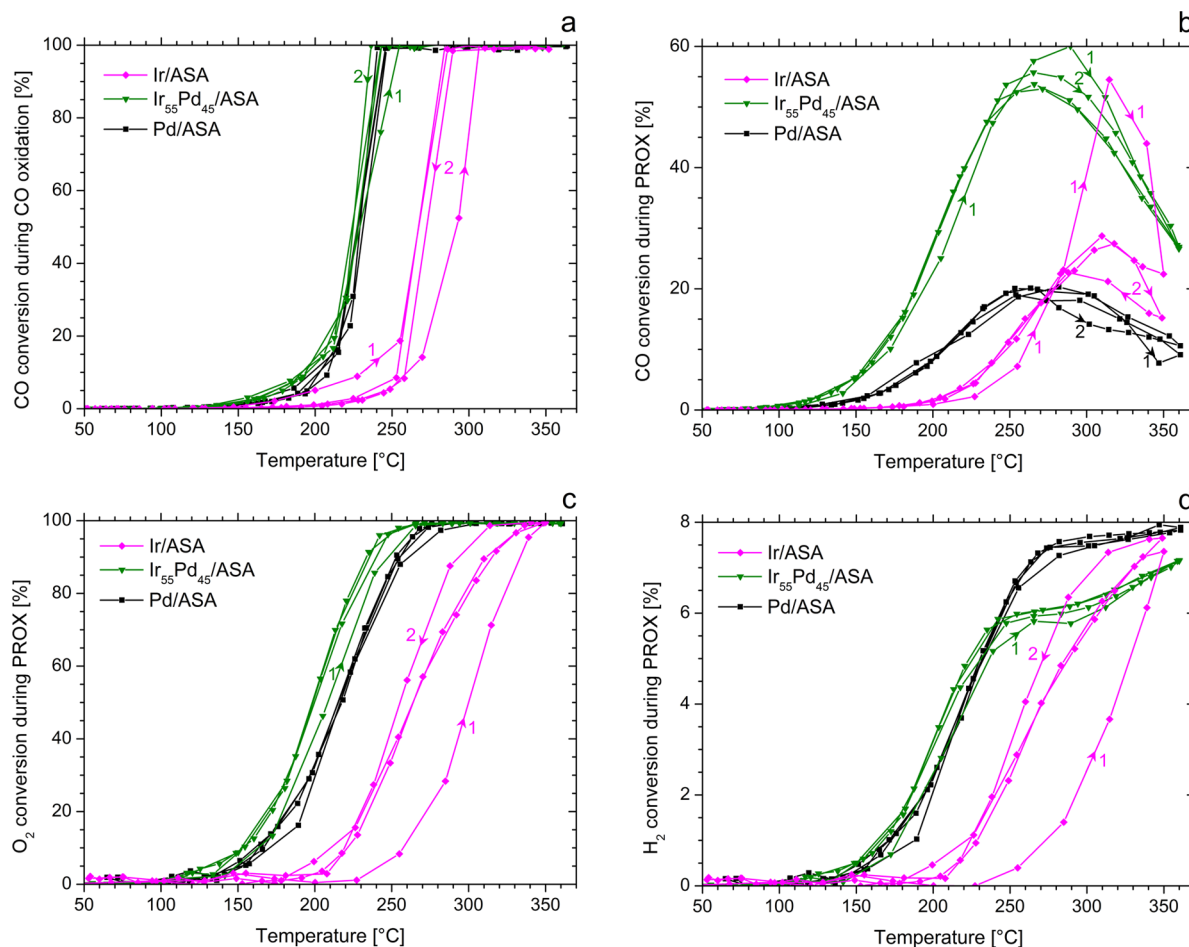


**Figure 1.** Reactant conversion vs temperature in  $\text{H}_2$ -free CO oxidation and PROX on Ir/ASA, IrPd/ASA, and Pd/ASA. The same number of metal atoms was used for all experiments. The temperature cycles are identified by numbers and arrows.

(Supporting Information, Figure S1). In addition, the behavior of alumina-supported catalysts is strikingly similar to that of the ASA-supported ones (compare Figure 1 to Supporting Information Figure S2).

From these results, it can be inferred that the particular behavior of Ir is due to its greater propensity to be oxidized, with respect to Pd. The  $\text{IrO}_2$  phase is thermodynamically more stable than the  $\text{PdO}$  one (see the Ellingham diagram of Supporting Information Figure S3). In addition, bulk Ir oxidation to  $\text{IrO}_2$  can proceed via a transient, metastable  $\text{Ir}_2\text{O}_3$  phase. Ir oxidation to  $\text{Ir}_2\text{O}_3$  occurs above  $\sim 300^\circ\text{C}$  in the 20–200 mbar  $\text{O}_2$  pressure range.<sup>26,29</sup> Moreover, as far as our catalysts are concerned, Ir-rich nanoparticles are most probably more easily oxidized than Pd-rich ones due to the smaller size of the former. Under PROX conditions, the first heating in a  $\text{H}_2$ -rich atmosphere may lead to an at least partial reduction of the Ir oxide likely formed during the previous CO oxidation cycles (starting from prereduced states), causing catalyst activation. It is likely that Ir phase transformations still occur during the second cycle (although to a smaller extent than in the first one), explaining why the CO conversions measured during the second cooling are different from those measured during the second heating.

To check these hypotheses, additional experiments were performed on Ir/ASA. They consisted of analyzing the effect of “true” reducing and oxidizing treatments on the cycle-dependent PROX kinetics. Figure 2a shows that a treatment

in  $\text{H}_2$  at  $400^\circ\text{C}$  leads to a small loop resembling the bottom loop exhibited by the classically treated catalyst (Figure 1b). This confirms that the high CO conversion (and selectivity to  $\text{CO}_2$ , not shown) first run in Figure 1b corresponds to an at least partially oxidized state, originating from the former CO oxidation cycles.

To go further, we submitted the catalyst to an  $\text{O}_2$  flow at  $350^\circ\text{C}$ . This generated a new behavior with a higher maximum CO conversion (Figure 2b), similar to the case of Figure 1b, run 1. This result supports the above hypothesis on the so-called “oxidic” character of the Ir nanoparticles after the CO oxidation cycles. Unlike in the standard protocol, the maximum CO conversion is reached at higher temperature ( $\sim 40^\circ\text{C}$ ), and the activity remains stable along the cycles (actually, the CO conversion is always slightly higher in the first run), which means that the oxidic phase is less stable than the oxide phase (i.e., the phase obtained after the oxidizing treatment).

To reinforce this argument and determine whether the oxidizing treatment is reversible, we exposed the Ir/ASA catalyst to an additional reducing treatment. Figure 2c shows that the loop behavior following the first reducing treatment is roughly retrieved. As a conclusion of these experiments, the Ir-rich nanoparticles encounter phase transformations in the course of the reaction cycles. CO oxidation conditions lead to an oxidic phase showing high maximum CO conversion in the first PROX run. In the subsequent PROX runs, the nano-

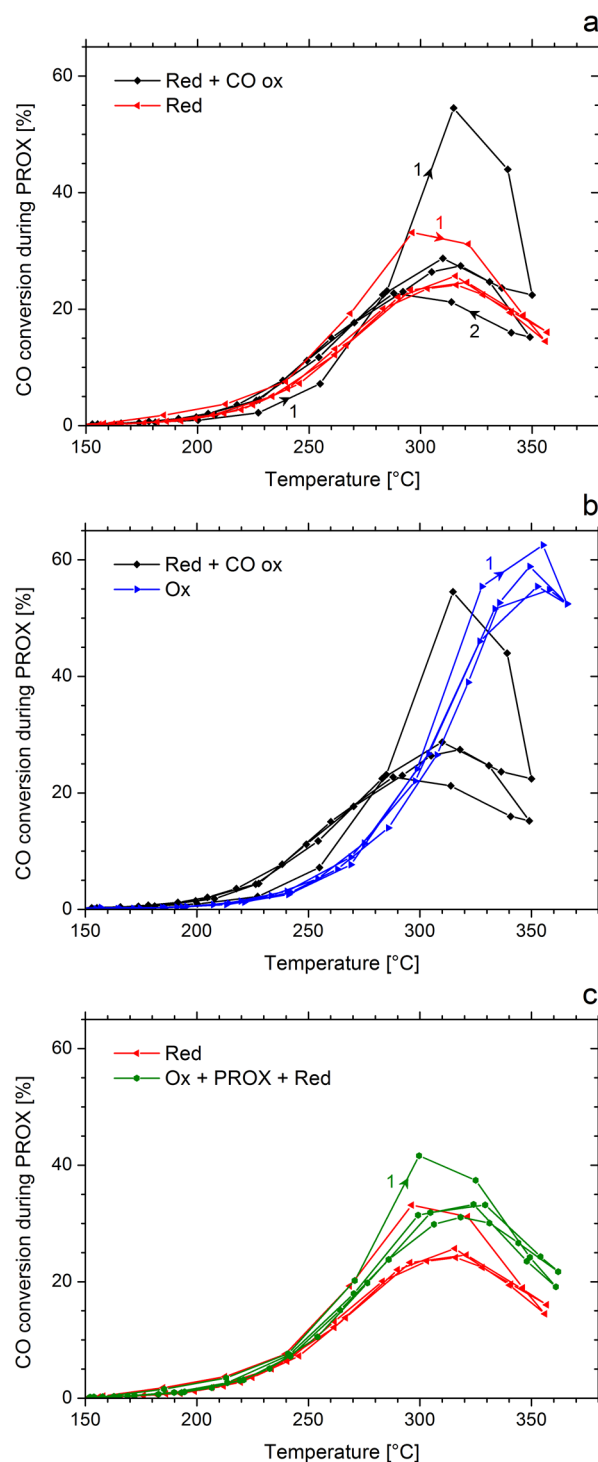


**Figure 2.** CO conversion in PROX as a function of temperature on Ir/ASA for various catalyst histories. (a) Classical treatment (reduction followed by two CO oxidation cycles) vs reduction pretreatment. (b) Classical treatment vs oxidation pretreatment. (c) Reduction pretreatment vs oxidation pretreatment followed by two PROX cycles and a reduction pretreatment. The temperature cycles are identified by numbers and arrows.

particles are reduced back and lose part of their preferential CO oxidation activity.

Starting now, we will focus on the last reaction run, that is, the cooling ramp of the second cycle, for each reaction. Figure 3 shows the CO conversion as a function of temperature during

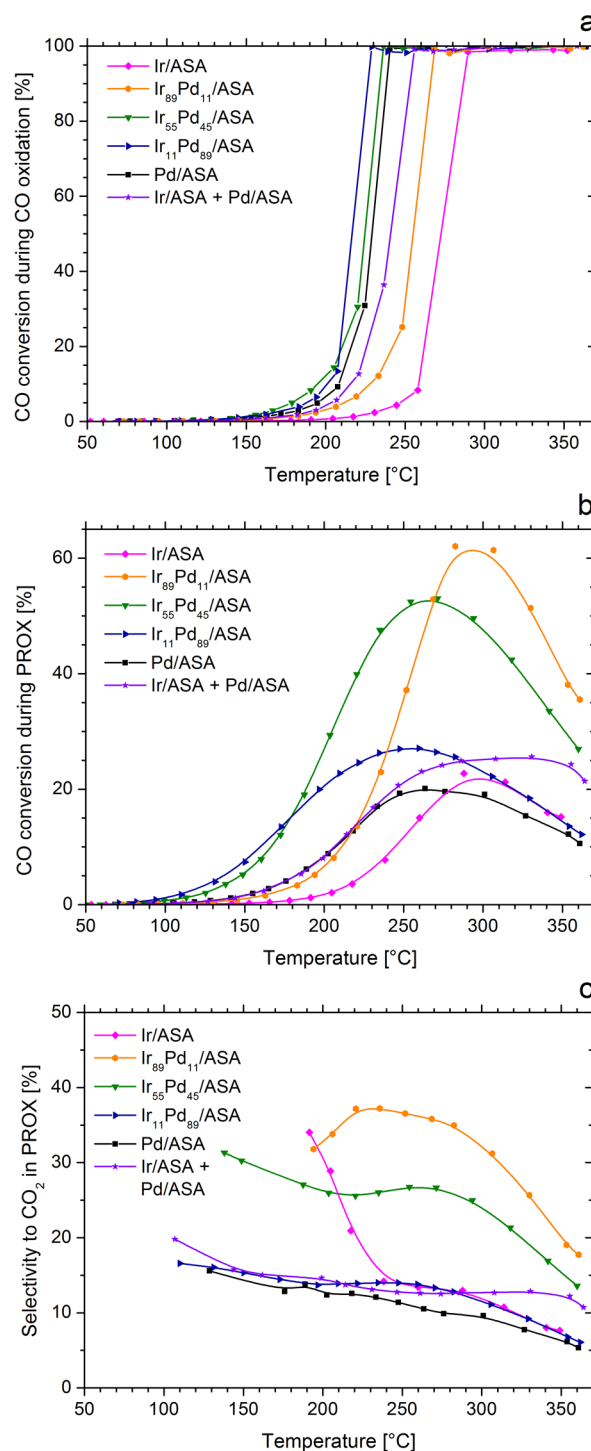


**Figure 3.** CO conversion vs temperature during H<sub>2</sub>-free CO oxidation (a) and PROX (b) on ASA-supported catalysts. Selectivity to CO<sub>2</sub> as a function of temperature in PROX (c). The selectivity to CO<sub>2</sub> is defined by the flow rate of produced CO<sub>2</sub> molecules divided by the total flow rate of produced molecules (CO<sub>2</sub> and H<sub>2</sub>O). The lines are guides to eye.

H<sub>2</sub>-free CO oxidation and PROX over all the ASA-supported catalysts described in Table 1 and an Ir/ASA + Pd/ASA mixture. Figure 4 allows a comparison between alumina and ASA-supported catalysts. The turnover frequencies (TOF, i.e., CO<sub>2</sub> formation rate in the light-off region normalized by the number of surface metal atoms calculated from the mean



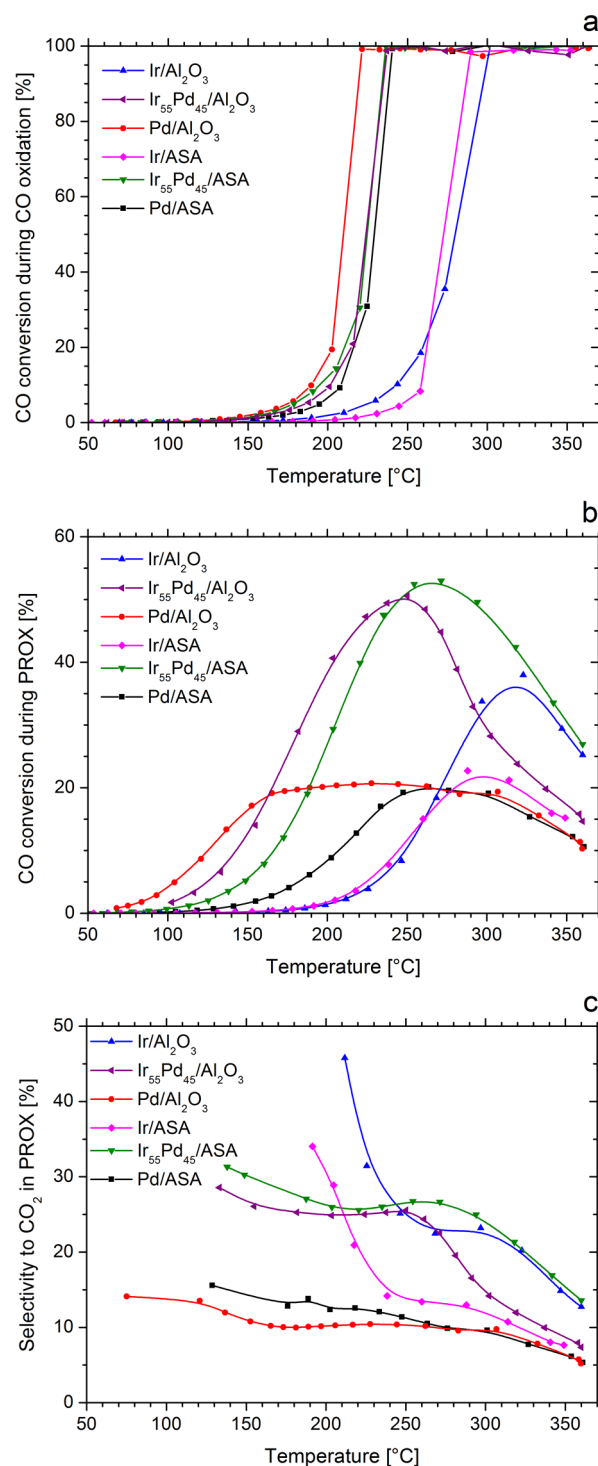


**Figure 4.** Same as Figure 3 for Ir, Ir<sub>55</sub>Pd<sub>45</sub>, and Pd catalysts.

particle size ( $d_{\text{surf}}$ ) are represented in Arrhenius plots in Figure 5 for all the catalysts.

**3.3. Activity in CO Oxidation and Effect of H<sub>2</sub>.** For H<sub>2</sub>-free CO oxidation, the following observations can be made: (i) the CO oxidation activity increases with the Pd content; (ii) IrPd/ASA is more active than the Ir/ASA + Pd/ASA mixture, which behaves roughly like Pd/ASA, taking the respective Pd amounts into account; and (iii) the support has only a slight influence on the activity. Because the light-off temperatures are strongly dependent on the CO adsorption energy (see below),

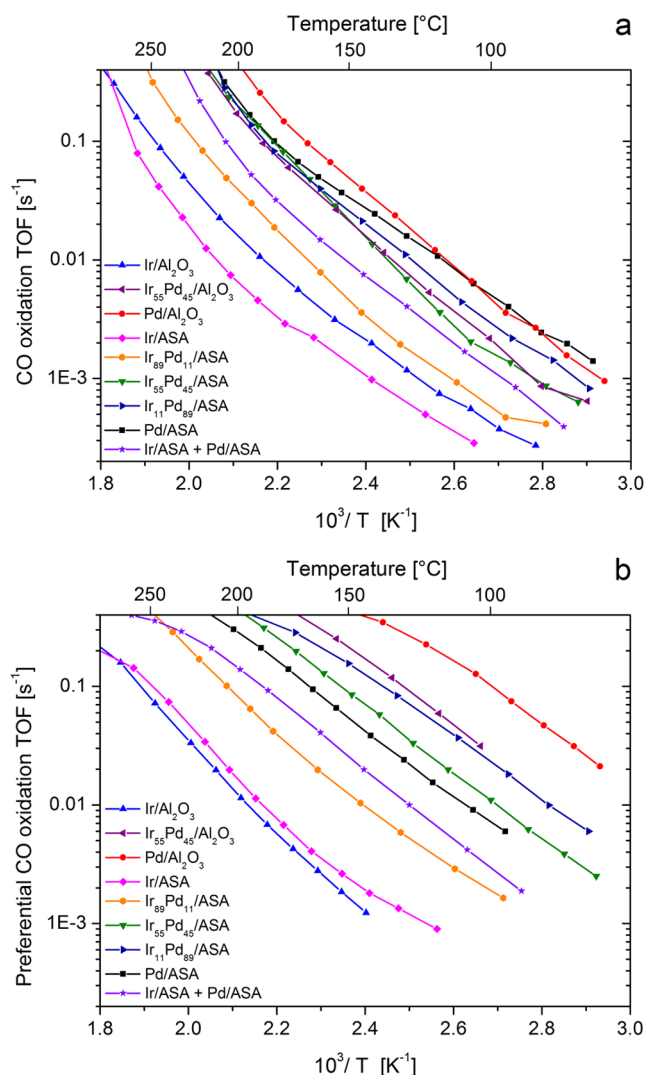


**Figure 5.** CO conversion turnover frequency (per number of surface metal atoms) vs temperature (Arrhenius plots) in H<sub>2</sub>-free CO oxidation (a) and PROX (b) on all the catalysts.

the latter result implies that, with respect to alumina, the acid sites of ASA do not significantly affect the surface electronic structure of the nanoparticles. This is supported by the fact that XPS analyses show a negligible 4f core level energy difference ( $\sim 0.3$  eV, within experimental error) between Ir/A and Ir/ASA (Supporting Information Figure S4).

Although similar trends are found for PROX, the range of activities is larger than that observed for H<sub>2</sub>-free CO oxidation (Figure 5b). Noticeably, the presence of H<sub>2</sub> generally induces an increase in the CO<sub>2</sub> formation rate. This boost is more important for alumina-supported Ir–Pd and Pd catalysts than for ASA-supported ones. At 150 °C, the greatest promotion is observed for IrPd/A, the CO oxidation TOF being multiplied by 10 in the presence of H<sub>2</sub> (versus 4 for IrPd/ASA).

**3.4. Selectivity.** As compared with light-off performances, under our conditions, the maximum CO conversions show a different hierarchy between the catalysts (Figures 3b and 4b). Strikingly, the CO conversion reached by the IrPd and Ir(Pd) catalysts is 51–62%, whereas the maximum conversion lies in the 20–38% range for the other ones. From the Ir/ASA + Pd/ASA mixture to the IrPd/ASA catalyst (Figure 3b), the

maximum conversion increases by 27%, and the temperature at maximum conversion decreases by 60 °C.

Let us analyze the influence of temperature on CO conversion. At low temperature, CO desorption is the rate-determining step; thus, more and more O<sub>2</sub> can be adsorbed as the temperature increases (and CO desorbs), leading to an increase in the CO conversion. In this regime, the competition between CO and hydrogen to react with oxygen does not depend on the temperature (stable selectivity, Figures 3c and 4c). At higher temperature, CO desorption becomes limiting, and the competition between CO and hydrogen becomes favorable to the latter (see the increase in H<sub>2</sub> conversion in Figure 1d and Supporting Information Figure S5b). This leads to a decrease in the CO conversion. In the particular case that O<sub>2</sub> conversion reaches 100% (Figure 1c and Supporting Information Figure S5a) below the critical CO desorption temperature (i.e. for the Pd catalysts, including the mixture), the limited oxygen supply gives rise to a plateau of CO conversion during PROX (Figures 3b and 4b). This feature is thus dependent on the reaction conditions. Indeed, experimental conditions similar to those described here, but using 5 times more IrPd/ASA catalyst, generate a CO conversion plateau (Supporting Information Figure S6), whereas it is not observed under standard conditions. In both cases, the selectivity to CO<sub>2</sub> is roughly constant up to the critical temperature of CO desorption.

Now we examine the CO<sub>2</sub> selectivity values (Figures 3c and 4c). It is seen that the Ir catalysts reach high selectivities (up to ~50%), but they correspond to negligible conversions (<5%) and decrease significantly when the temperature increases. The selectivities of the Pd-rich catalysts (Pd concentration > 50%) and the Ir/ASA + Pd/ASA mixture are rather stable but low, with values between 10 and 20% below 300 °C. Note that the mixture behaves roughly like Pd/ASA, which is the most active component. Mariño et al. have also reported on the higher selectivity and lower activity of supported Ir catalysts as compared with Pd ones.<sup>7</sup> For IrPd and Ir(Pd) catalysts, the selectivities reach ~29–37% and correspond to high CO conversions. Ir<sub>89</sub>Pd<sub>11</sub>/ASA is the most efficient catalyst in terms of maximum selectivity to CO<sub>2</sub> and maximum CO conversion, but its selectivity decreases below 220 °C. Conversely, the selectivity of the IrPd catalysts remains somewhat constant between 130 and 270 °C.

## 4. DISCUSSION

### 4.1. Support-Dependent Promoting Effect of H<sub>2</sub>.

Several authors have reported a promotional effect of H<sub>2</sub> on CO oxidation over Pt/Al<sub>2</sub>O<sub>3</sub> (ref 30 and references therein) and Pd/Al<sub>2</sub>O<sub>3</sub>.<sup>3,31</sup> For such platinum-group metals, the explanations all invoke a H<sub>2</sub>-induced desorption of CO, via either lowering of the metal–CO bond from H coadsorption or CO-consuming formate production on the hydroxylated support, or temperature release from H<sub>2</sub> oxidation. Indeed, CO desorption, which is known to be the rate-determining step near the light-off temperature in H<sub>2</sub>-free CO oxidation, enables dissociative adsorption of O<sub>2</sub> and the subsequent CO + O reaction.<sup>32</sup> On the basis of the similar apparent activation energies for H<sub>2</sub>-free CO oxidation (20–31 kJ mol<sup>-1</sup>) and CO PROX (23–31 kJ mol<sup>-1</sup>) determined from Figure 5, it is likely that no critical change in the reaction mechanism occurs upon H<sub>2</sub> addition. Thus, the promotion of CO desorption is a possible explanation for the H<sub>2</sub>-induced boost of CO oxidation in the present case. However, depending on the adsorption

competition between species, CO desorption could instead favor H<sub>2</sub> oxidation at the expense of PROX selectivity.

We have previously reported on the promotional effect of hydrogen in PROX for gold catalysts and ascribed it to the formation of oxidative species, namely, OH and OOH intermediates, due to the copresence of O<sub>2</sub> and H<sub>2</sub> (ref 33 and references therein). Similarly, Liu et al. have suggested a CO + OH PROX pathway on Ir–Fe/SiO<sub>2</sub>.<sup>13</sup> Mechanisms involving hydroxyl or hydroperoxy groups have also been proposed for modified Pt-based catalysts.<sup>34,35</sup> We believe that an OH/OOH-mediated mechanism cannot be ruled out in the case of supported Ir–Pd nanoalloys. According to our proposed mechanism for gold,<sup>33</sup> the active OH/OOH intermediates are formed on the metal and also react on it. Extrapolating to Pt-group metals, an additional supply of hydroxyl species from the support would increase the CO PROX rate under certain conditions<sup>2</sup> but would not significantly affect the reaction mechanism.

Whatever the interpretation, the differences between alumina and ASA-supported catalysts in PROX suggest that mobile surface hydroxyl groups play a role in the promotion by H<sub>2</sub>. The smaller amount of basic OH species on ASA<sup>24</sup> may explain the greater promotion of CO oxidation on the alumina-supported catalysts. Note that the higher surface area of ASA with respect to alumina (factor of ~2) may also play a role, but with respect to the promotion of metal-catalyzed CO oxidation, the density of OH groups in the vicinity of the particles is more critical than their total amount. The nature of the support could also influence the reactions via a different surface diffusivity of the adsorbates (spillover). In addition, the structure of the supported particles may be different between ASA and alumina supports. However, in the latter two cases, H<sub>2</sub>-free CO oxidation would also be affected.

**4.2. Nanoalloying Effect.** Alloying selective Ir and highly active Pd leads to a true synergistic effect on the PROX performances. As evidenced elsewhere for gold catalysts,<sup>36</sup> it is shown here for Ir and Pd catalysts that the most efficient ones in H<sub>2</sub>-free CO oxidation are not necessarily the best ones in PROX. The origin of the alloying effect is presently unknown. Classical interpretations invoke geometric vs electronic alloying effects.<sup>17</sup> The chemical structure of IrPd nanoalloys is currently undetermined due to the lack of investigations with advanced techniques such as in situ EXAFS, aberration-corrected TEM, or DFT calculations. According to thermodynamics for bulk solids in the absence of adsorbed phase, the Ir–Pd binary phase diagram presents a large miscibility gap, that is, the absence of alloying above a composition of ~10% Pd at moderate temperature.<sup>37</sup> Moreover, the surface energy of Pd (2.1 J m<sup>-2</sup>) is much lower than that of Ir (3.0 J m<sup>-2</sup>),<sup>38</sup> and the atomic sizes are similar (relative difference of lattice parameter, 1.3%). This suggests surface segregation of Pd, as confirmed experimentally for Ir/Pd<sup>39</sup> and Pd/Ir<sup>40</sup> surface deposits. This indicates that the separation in two pure bulk phases expected for the bulk IrPd alloy could be replaced in small clusters by an Ir@Pd core–shell structure induced by surface–volume phase separation and surface segregation of Pd atoms.<sup>41</sup> In this case, the high selectivity of the IrPd catalysts could be due to the so-called ligand effect caused by the Ir-rich subsurface on the electronic properties of surface Pd atoms, modifying the adsorption strength of reactants with respect to pure Pd.

To support these considerations, XPS was performed on Ir/ASA and IrPd/ASA after in situ reduction. The Pd 3d regions of XPS spectra show a small positive shift of ~0.2 eV going

from Pd to IrPd (Supporting Information Figure S7). Using XPS, Schwarz et al. have studied thin alloyed Pd<sub>75</sub>Ir<sub>25</sub> and Pd<sub>25</sub>Ir<sub>75</sub> films obtained by electron-beam coevaporation in an ultrahigh vacuum system.<sup>40</sup> They have reported large positive shifts of 0.40 and 0.85 eV, respectively, for the Pd 3d core levels with respect to the pure bulk phase. Assuming a linear dependence of this shift with the composition, one can predict a value of 0.7 eV for an Ir<sub>55</sub>Pd<sub>45</sub> alloy. On the other hand, Pd 3d surface core-level shifts of −0.44 eV and −0.55 eV have been reported for the Pd (100) and (110) surfaces, respectively.<sup>42</sup> These values are of opposite sign and only slightly smaller than the shift expected from the alloying effect. On the basis of these data, adding the opposite contributions of alloying and surface effects, the shift obtained for our system should be equal to ~0.2 eV, which is exactly the case. Hence, it is compatible with an Ir@Pd core–shell structure.

In the case of the CO/Pd system, positive core-level shifts observed for Pd overlayers have been shown to correspond to a decreased chemisorption energy of CO with respect to Pd single crystals.<sup>43,44</sup> Hence, the better PROX performances of IrPd particles over Pd ones could originate from the softer bonding of CO as well as the changes in the bonding strength of other adsorbates. This type of argument was also used to explain the enhanced PROX activity of Ru@Pt core–shell nanoparticles, which would contain more CO-free Pt surface sites than their pure Pt counterparts.<sup>34</sup>

The presence of H<sub>2</sub> during PROX should not modify the possible Ir@Pd structure because the H–Pd bond is slightly stronger than the H–Ir one.<sup>45</sup> Moreover, the adsorption of O<sub>2</sub> on an Ir–Pd surface does not favor Ir segregation.<sup>39</sup> However, dissolution of hydrogen in Pd compounds can cause lattice rearrangements.<sup>46</sup> Following this idea, an alternative or complementary explanation of the alloying effect could be the Ir-induced inhibition of hydrogen dissolution in the Pd-containing particles. As a matter of fact, Pd hydride formation was shown to be detrimental to selective CO oxidation because of the high reactivity of hydride hydrogen toward oxygen.<sup>9</sup>

## 5. CONCLUSIONS

A series of Ir, Pd, and Ir–Pd nanoalloys supported on  $\gamma$ -alumina and amorphous silica–alumina has been synthesized by incipient wetness (co)impregnation of acetylacetonate(s), followed by reduction in hydrogen.

The catalysts have been tested in H<sub>2</sub> oxidation, H<sub>2</sub>-free CO oxidation, and PROX in a flow fixed-bed microreactor (CO/O<sub>2</sub>/H<sub>2</sub> = 2:2:48 vol %, atmospheric pressure). In the course of the two heating–cooling cycles performed in both CO oxidation and PROX, the Ir-rich catalysts exhibited a complex cycling behavior, unlike the Pd-rich ones. From specific experiments on preoxidized and prereduced catalysts, this is ascribed to reaction conditions-dependent phase change originating from the greater sensitivity of Ir-rich nanoparticles to oxidation, as compared with Pd-rich ones.

The addition of H<sub>2</sub> to the CO oxidation stream induces an increase in the turnover frequencies of CO<sub>2</sub> formation. Along with the classically invoked H<sub>2</sub>-induced CO desorption, a possible effect of species formed from H<sub>2</sub>–O<sub>2</sub> combination on CO oxidation activity is alternatively envisaged to explain the promoting effect of H<sub>2</sub>. This is consistent with the fact that alumina-supported Ir–Pd and Pd catalysts are more promoted than acidic ASA-supported ones. Conversely, from the similar kinetics observed for alumina and ASA-supported catalysts in

H<sub>2</sub>-free CO oxidation, it is concluded that the support acidity does not play a significant role in this reaction.

The turnover frequencies in CO oxidation and PROX generally increase with the Pd content of the catalysts. However, in PROX, the IrPd catalysts reveal a marked superiority over their pure metal counterparts and an Ir + Pd mechanical mixture in terms of CO conversion (up to 53% for the Ir<sub>45</sub>Pd<sub>55</sub> composition in our conditions, which is about twice the value obtained for Ir and Pd catalysts) and selectivity. Indeed, for significant CO conversions, the CO<sub>2</sub> selectivity of IrPd catalysts reaches the highest value (26% vs less than 13% for the other catalysts, at 250 °C) and is stable in the ~100–300 °C range.

This remarkable alloying effect is ascribed to (i) an Ir-induced inhibition of hydrogen dissolution in the Pd-containing particles, hydride formation being detrimental to PROX, (ii) a charge transfer between the core and the shell of the Ir@Pd particles, or both. The hypothetical core–shell structure, which is consistent with thermodynamics and XPS data, will be investigated in more detail in a future work.

## ■ ASSOCIATED CONTENT

### Supporting Information

The file contains additional catalytic results as well as XPS and thermodynamic data (Figures S1–S7). This material is available free of charge via the Internet at <http://pubs.acs.org>.

## ■ AUTHOR INFORMATION

### Corresponding Author

\*E-mail: [laurent.piccolo@ircelyon.univ-lyon1.fr](mailto:laurent.piccolo@ircelyon.univ-lyon1.fr).

### Notes

The authors declare no competing financial interest.

## ■ ACKNOWLEDGMENTS

The authors acknowledge N. Cristin and P. Mascunari (ICP), M. Aouine and L. Burel (TEM-EDX), and P. Delichère and L. Massin (XPS) for their help in sample characterization. L. Piccolo and F. Morfin acknowledge financial support by the French National Research Agency (ANR) through the DINAMIC project. L. Piccolo acknowledges the European COST Action MP0903 Nanoalloy for fruitful network discussions.

## ■ REFERENCES

- (1) Park, E. D.; Lee, D.; Lee, H. C. *Catal. Today* **2009**, *139*, 280–290.
- (2) Liu, K.; Wang, A.; Zhang, T. *ACS Catal.* **2012**, *2*, 1165–1178.
- (3) Stetter, J. R.; Blurton, K. F. *Ind. Eng. Chem. Prod. Res. Dev.* **1980**, *19*, 214–215.
- (4) Oh, S. H.; Sinkevitch, R. M. *J. Catal.* **1993**, *142*, 254–262.
- (5) Li, W.; Gracia, F. J.; Wolf, E. E. *Catal. Today* **2003**, *81*, 437–447.
- (6) Rosso, I.; Galletti, C.; Saracco, G.; Garrone, E.; Specchia, V. *Appl. Catal., B* **2004**, *48*, 195–203.
- (7) Mariño, F.; Descorme, C.; Duprez, D. *Appl. Catal., B* **2004**, *54*, 59–66.
- (8) Hultberg, P. C.; Brandin, J. G. M.; Silversand, F. A.; Lundberg, M. *Int. J. Hydrogen Energy* **2005**, *30*, 1235–1242.
- (9) Pozdnyakova, O.; Teschner, D.; Wootsch, A.; Kröhnert, J.; Steinhauer, B.; Sauer, H.; Toth, L.; Jentoft, F. C.; Knop-Gericke, A.; Paál, Z.; Schlögl, R. *J. Catal.* **2006**, *237*, 17–28.
- (10) Boronin, A. I.; Slavinskaya, E. M.; Danilova, I. G.; Gulyaev, R. V.; Amosov, Y. I.; Kuznetsov, P. A.; Polukhina, I. A.; Koscheev, S. V.; Zaikovskii, V. I.; Noskov, A. S. *Catal. Today* **2009**, *144*, 201–211.
- (11) Miguel-García, I.; Berenguer-Murcia, Á.; Cazorla-Amorós, D. *Appl. Catal., B* **2010**, *98*, 161–170.



- (12) Huang, Y.; Wang, A.; Wang, X.; Zhang, T. *Int. J. Hydrogen Energy* **2007**, *32*, 3880–3886.
- (13) Liu, K.; Wang, A.; Zhang, W.; Wang, J.; Huang, Y.; Wang, X.; Shen, J.; Zhang, T. *Ind. Eng. Chem. Res.* **2011**, *50*, 758–766.
- (14) Piccolo, L.; Nassreddine, S.; Morfin, F. *Catal. Today* **2012**, *189*, 42–48.
- (15) Sinfelt, J. H. *Bimetallic Catalysts: Discoveries, Concepts, and Applications*; Wiley: New York, 1983.
- (16) Poncet, V.; Bond, G. C. *Catalysis by Metals and Alloys; Studies in Surface Science and Catalysis*; Elsevier: Amsterdam, 1995.
- (17) Piccolo, L. Surface studies of catalysis by metals: Nanosize and alloying effects. In *Nanoalloys: Synthesis, Structure and Properties*; Alloyeau, D., Mottet, C., Ricolleau, C., Eds.; Springer: London, 2012.
- (18) Piccolo, L.; Nassreddine, S.; Aouine, M.; Geantet, C.; Ulhaq, C. *J. Catal.* **2012**, *292*, 173–178.
- (19) Coq, B.; Figueras, F. *J. Mol. Catal., A* **2001**, *173*, 117–134.
- (20) Persson, K.; Ersson, A.; Jansson, K.; Iverlund, N.; Järås, S. *J. Catal.* **2005**, *231*, 139–150.
- (21) López-De Jesús, Y. M.; Johnson, C. E.; Monnier, J. R.; Williams, C. T. *Top. Catal.* **2010**, *53*, 1132–1137.
- (22) Shen, S. Y.; Zhao, T. S.; Xu, J. B. *Electrochim. Acta* **2010**, *55*, 9179–9184.
- (23) Rocha, A. S.; Moreno, E. L.; da Silva, G. P. M.; Zotin, J. L.; Faro, A. C., Jr. *Catal. Today* **2008**, *133–135*, 394–399.
- (24) Daniell, W.; Schubert, U.; Glöckler, R.; Meyer, A.; Noweck, K.; Knözinger, H. *Appl. Catal., A* **2000**, *196*, 247–260.
- (25) Nassreddine, S.; Casu, S.; Zotin, J. L.; Geantet, C.; Piccolo, L. *Catal. Sci. Technol.* **2011**, *1*, 408–412.
- (26) Nassreddine, S.; Bergeret, G.; Jouguet, B.; Geantet, C.; Piccolo, L. *Phys. Chem. Chem. Phys.* **2010**, *12*, 7812–7820.
- (27) Nassreddine, S.; Massin, L.; Aouine, M.; Geantet, C.; Piccolo, L. *J. Catal.* **2011**, *278*, 253–265.
- (28) Piccolo, L.; Nassreddine, S.; Toussaint, G.; Geantet, C. *ChemSusChem* **2012**, *5*, 1717–1723.
- (29) He, Y. B.; Stierle, A.; Li, W. X.; Farkas, A.; Kasper, N.; Over, H. *J. Phys. Chem. C* **2008**, *112*, 11946–11953.
- (30) Salomons, S.; Hayes, R. E.; Votsmeier, M. *Appl. Catal., A* **2009**, *352*, 27–34.
- (31) Muraki, H.; Matunaga, S.; Shinjoh, H.; Wainwright, M. S.; Trimm, D. L. *J. Chem. Technol. Biotechnol.* **1991**, *52*, 415–424.
- (32) Engel, T.; Ertl, G. *Adv. Catal.* **1979**, *28*, 1–78.
- (33) Quinet, E.; Piccolo, L.; Morfin, F.; Avenier, P.; Diehl, F.; Caps, V.; Rousset, J. L. *J. Catal.* **2009**, *268*, 384–389.
- (34) Nilekar, A. U.; Alayoglu, S.; Eichhorn, B.; Mavrikakis, M. *J. Am. Chem. Soc.* **2010**, *132*, 7418–7428.
- (35) Tanaka, K.; He, H.; Shou, M.; Shi, X. *Catal. Today* **2011**, *175*, 467–470.
- (36) Rossignol, C.; Arrii, S.; Morfin, F.; Piccolo, L.; Caps, V.; Rousset, J. L. *J. Catal.* **2005**, *230*, 476–483.
- (37) Tripathi, S. N.; Bharadwaj, S. R.; Chandrasekharaiah, M. S. *J. Phase Equilib.* **1991**, *12*, 603–605.
- (38) Boer, F. R.; de Boom, R.; Mattens, W. C. M.; Miedema, A. R.; Niessen, A. K. *Cohesion in Metals: Transition Metal Alloys*; North-Holland Physics Publishing: Amsterdam, 1989.
- (39) Aas, N.; Bowker, M. *Surf. Sci.* **1994**, *310*, 113–127.
- (40) Schwarz, R. B.; Harms, U.; Jain, H. *Mater. Sci. Eng., A* **2004**, *375–377*, 194–200.
- (41) Rousset, J. L.; Cadete Santos Aires, F. J.; Sekhar, B. R.; Mélinon, P.; Prevel, B.; Pellarin, M. *J. Phys. Chem. B* **2000**, *104*, 5430–5435.
- (42) Andersen, J. N.; Hennig, D.; Lundgren, E.; Methfessel, M.; Nyholm, R.; Scheffler, M. *Phys. Rev. B* **1994**, *50*, 17525–17533.
- (43) Rodriguez, J. A.; Goodman, D. W. *Science* **1992**, *257*, 897–903.
- (44) Hammer, B.; Morikawa, Y.; Nørskov, J. K. *Phys. Rev. Lett.* **1996**, *76*, 2141–2144.
- (45) Alfonso, D. R. *Surf. Sci.* **2008**, *602*, 2758–2768.
- (46) Flanagan, T. B.; Park, C.-N. *J. Alloys Compd.* **1999**, *293–295*, 161–168.